Size-Dependent Energy of Ni Nanoparticles on Graphene Films on Ni(111) and Adhesion Energetics by Adsorption Calorimetry

John R. Rumptz[1†], Kun Zhao[2†], Jackson Mayo[2], and Charles T. Campbell[1,2,*]
[1]Department of Chemical Engineering, and [2]Department of Chemistry
University of Washington
Seattle, Washington 98105-1700, USA

Abstract

The use of carbon supports for late transition metal nanoparticle catalysts has grown substantially in recent years due to efforts to develop electrocatalysts for clean energy applications and catalysts for new aqueous-phase biomass-related conversions, and due to the evolution of new carbon materials with unique properties (e.g., graphene, carbon nanotubes, etc.). However, much less is known about the bonding energetics of catalytic metal nanoparticles on carbon supports in comparison with oxide supports, which are more common for thermal catalysis. Here we report the growth morphology and heats of adsorption of Ni vapor deposited onto graphene/Ni(111) at 300 K and 100 K using metal vapor single crystal adsorption calorimetry (SCAC) and He^+ low-energy ion scattering (LEIS). These results provide the Ni chemical potential versus particle size and the Ni / graphene adhesion energy. LEIS intensities suggest that Ni grows as flat-topped FCC islands with a nearly constant thickness of ~1.5 nm when deposited at 300 K. At 100 K, Ni grows as smaller nanoparticles, well modeled as hemispherical HCP nanoparticles with a density of ~2×10^{16} particles/m^2. The Ni chemical potential as a function of average particle diameter in the 0.5 to 4 nm range at 100 K was determined from the heats of Ni gas adsorption. By fitting the measured chemical potential as a function of diameter, we determined an adhesion energy of 3.6 J/m^2 for large Ni particles on graphene/Ni(111). This adhesion energy is in good agreement with previous STM and DFT investigations of Ni/graphene/Ni(111).

* Corresponding author: charliec@uw.edu

† John Rumptz and Kun Zhao contributed equally to this work.

Keywords: metal adsorption energy, supported nanoparticles, carbon supports, metal chemical potential, particle / support interactions, adsorption calorimetry, ion scattering spectroscopy

1. Introduction

Late transition metal nanoparticles anchored to high-surface-area support materials are widely used as heterogeneous catalysts and electrocatalysts for energy, environmental, and chemical applications. The adsorption energies of small molecules and reaction intermediates onto the metal nanoparticles greatly affect the activity and selectivity of these catalysts. It is well-known that these adsorption energies and the catalyst thermal stability are strongly influenced by the size of the metal nanoparticles as well as the support material to which the nanoparticles bind.[1–7] Thus, a fundamental understanding of these nanoparticle size and support effects is important to designing improved catalysts. Previous work by our group has shown that the chemical potential of metal atoms in supported nanoparticles contains important information about both these particle size and support effects in catalysis.[2,8,9] That work demonstrated that the metal chemical potential can be modelled as a function of the nanoparticle size and the adhesion energy of the metal to the support material.[2,8] A higher chemical potential leads to stronger adsorption of small molecules and intermediates as well as a larger driving force for catalyst deactivation via sintering.[2,9,10]

Carbon supports are important and widely used for heterogeneous catalysts, electrocatalysts, and photocatalysts due to carbon's resistance to chemical degradation, high-temperature stability, simple fabrication methods, low cost, and high electrical conductivity.[11–14] While there is a wide variety of carbon-based support materials (e.g. activated carbon, carbon black, graphite), many of these materials share the same graphitic building block.[13] The interesting chemical properties and applications of graphitic carbon in heterogeneous catalysis make it an appealing template for fundamental research. Here we measure the chemical potential of Ni atoms in Ni nanoparticles supported on a graphene film on Ni(111), and show how the chemical potential relates quantitatively to particle size via the Ni / graphene adhesion energy.

Recently, our group studied the energetics of Ag atoms and nanoparticles on graphene supported on Ni(111).[15] That was the only previous study of metal atom energetics for any late transition metal on any carbon support material. The Ag monomer was found to bind more weakly to graphene than it does to the surfaces of metal oxide supports. It was also found that Ag nanoparticles have a lower adhesion energy (in the large-size limit) to graphene/Ni(111) than onto reducible metal oxides such as CeO_2(111) and TiO_2(100), but higher adhesion energy than on irreducible metal oxides such as MgO(100). The bonding of Ag to the graphene support is somewhat unique in combining weak monomer bonding with moderately strong nanoparticle adhesion, which has advantages as a catalyst support.[15] This motivates the investigation of other later transition metals on graphene.

Nickel based heterogeneous catalysts are important for a wide variety of chemical reactions.[16–21] It is also well-known that the selectivity of these Ni catalysts is strongly affected by size and support material.[22–25] For example, in CO_2 hydrogenation on Ni catalysts, small molecules such as CO and CH_4 dominate on small nanoparticles, while carbon-carbon chain

formation requires larger particles with available neighboring sites for C-C coupling.[24,25] For this same reaction, different metal oxide supports vary the hydrogenation products via binding different intermediates.[24,25]

Nickel nanoparticles supported on graphitic materials are used as an alternative to expensive platinum-based electrocatalysts for oxidation reactions.[26–29] It has been shown that the nature of the interaction of the Ni nanoparticles with the carbon support can have a large influence on the reactivity of these catalysts.[28–30] In addition, it is well-known that the particle size can have a major effect on the catalyst kinetics for Pt-group metals.[24,31–35]

There are many excellent theoretical (mostly DFT) calculations of the bonding strength between Ni and graphitic materials[36–41] and experimental measurements of the particle morphology of Ni on graphitic supports.[36,42–44] While the exact details of these studies can vary tremendously, there is some consensus that Ni forms strong bonds with C(0001) and clustering of Ni monomers leads to the formation of 3D Ni particles on graphite and graphene.[36,38–43] Despite all the previous work done investigating the surface science of Ni on C(0001), to our knowledge there is only one experimental measurement of the bonding strength between Ni and a graphitic support, whereby an adhesion energy of 3.5 J/m^2 at the Ni/graphene interface was estimated from the shape of graphene-supported Ni nanoparticles.[36]

In this paper, we report the bonding energetics of Ni atoms in Ni nanoparticles grown by Ni vapor deposition onto a graphene-covered Ni(111) support using single crystal adsorption calorimetry (SCAC). These measurements determined the heat of adsorption of Ni vapor atoms as they adsorb onto the graphene substrate and bond to previous formed Ni nanoparticles of controlled size. The growth morphology of this vapor deposited Ni was measured using low-energy ion scattering (LEIS). From the coverage dependent heats of adsorption and particle size from LEIS, we determined the chemical potential as a function of the average Ni particle diameter and the adhesion energy of Ni to graphene/Ni(111). The results presented here provide important details of the chemical bonding energetics of Ni nanoparticles to metal-supported graphene support materials. To our knowledge, this paper presents the only measurement of Ni chemical potential versus Ni nanoparticle size on any well-defined carbon-based support, and the first calorimetric measurement of the adhesion energy of Ni nanoparticles to any well-defined carbon-based support. This is just a first step in understanding how Ni chemical potential relates to the performance of Ni catalysts on carbon supports. Because of the cleanliness and order of this Ni(111) supported graphene surface, the results also serve as an energy benchmark for comparison to density functional theory (DFT) calculations with different functionals, as a means to validate the functional's energy accuracy with respect to metal nanoparticle bonding to carbon-based supports.

2. Experimental Methods

A full description of the single-crystal adsorption calorimetry (SCAC) apparatus and detailed experimental procedures is presented elsewhere.[45] Briefly, the calorimetry experiments were done in an ultrahigh-vacuum (UHV) chamber with a base pressure $<2 \times 10^{-10}$ Torr. This chamber is also equipped with X-ray photoelectron spectroscopy (XPS), Auger electron spectroscopy (AES), He^+ low-energy ion scattering (LEIS), low-energy electron diffraction (LEED), quadrupole mass spectrometry (QMS), and two quartz crystal microbalances (QCMs). Surface spectroscopy measurements were obtained with a PHI 10−360 precision energy analyzer with a PHI 72−250 position sensitive detector.

The Ni metal beam is generated by evaporating Ni pellets in an e-beam evaporator. The Ni vapor is collimated through a series of apertures to give an average beam diameter of 4.26 mm. The beam is then pulsed with a chopper with a pulse duration of 100 ms and a period of 2 s. The Ni flux is monitored with two QCMs: one on-axis QCM to measure the flux at the sample position (possible only just before and just after calorimetry) and another off-axis QCM to continuously monitor the flux during the experiment. The flux varies with time (typically dropping by ∼10% during a run), so the continuously measured off-axis flux was scaled at all times in a method described previously to provide the flux at all times at the sample position.[45]

The heat released is measured using a pyroelectric polyvinylidene fluoride (PVDF) ribbon in thermal and mechanical contact with the 1 μm thick Ni(111) single-crystal sample. The PVDF ribbon is calibrated for each experiment using a HeNe laser with known energy. The total heat detected with the PVDF ribbon is a combination of the heat of adsorption as well as the thermal radiation from the hot metal source. The signal from thermal radiation was measured by placing a barium fluoride (BaF_2) window in front of the sample to block Ni atoms from reaching the sample but allowing a known fraction of thermal radiation to transmit through the window (>90%, measured with and without the window in the path). The resulting signal from thermal radiation was then subtracted from the total heat signal. The measured heat was further corrected to account for the difference in internal (translational) energy between the directed flux of gas-phase Ni atoms coming from the high-temperature electron beam evaporator (∼2000 K)[22] and a collection of the same gas atoms in a Boltzmann distribution at the surface temperature (300 or 100 K).[46] The resulting heat is thereby equal to the negative of the standard enthalpy of Ni adsorption at the sample temperature.

The sticking probability of each pulse is measured simultaneously with the adsorption heats using a modified King and Well's method described previously.[45,47] The number of Ni atoms that stick to the sample surface in each pulse is then equal to the flux times the pulse duration and the sticking probability. The differential heat of adsorption per mole of adsorbed Ni as a function of the cumulative Ni coverage can then be calculated from the measured heats, fluxes, and sticking probabilities. The Ni coverages reported here are given in units of monolayers (ML), with 1 ML defined as 1.87×10^{19} atoms/m^2, which is the areal density of Ni

atoms on the Ni(111) surface as well as exactly ½ the areal density of C atoms on the graphene surface, which grows in registry with the Ni(111) substrate.[48,49]

3. Results

3.1 Graphene Growth and Characterization

Graphene films were grown on a clean 1 μm thick Ni(111) single crystal sample using a direct growth method from ethene gas previously described in the literature.[15,36,50,51] This procedure is known to produce a single layer of graphene on Ni(111) and not multilayers nor multilayer islands.[36,50,51] Before growth, the Ni(111) sample was cleaned by cycles of flashing the sample at 800ºC followed by 1.0 kV Ar^+ ion sputtering until the presence of the C 1s carbon peak could no longer be detected by XPS. The clean Ni(111) sample was then annealed in vacuum at 600-650ºC for 5 min before the sample was exposed to 10^{-6} Torr of ethylene for 30 min while the sample was continually held at 600-650ºC. After growth the presence of graphene was confirmed by AES. Previous work has shown that the C-KVV AES line has distinctive shapes for graphitic or carbidic carbon which provided an easy method to determine the surface carbon phase.[36,52,53] In line with previous work, we found that samples grown at temperatures below 500ºC showed the presence of nickel carbide while samples grown between 600 and 650ºC consistently showed the line-shape characteristic of graphene.[36] The quality of all graphene films was further confirmed with He^+ LEIS in this study, which was quantified by the ratio of the nickel LEIS signal from the sample after graphene growth to that from the clean Ni(111). This ratio showed that the graphene films covered >95% of the Ni(111) surface for all samples investigated here.

3.2 Ni Sticking Probability on Graphene/Ni(111)

The sticking probability of Ni gas atoms to graphene/Ni(111) was monitored during calorimetry experiments by measuring the transient QMS signal for Ni atoms during each deposited pulse of the atomic beam. This signal was then normalized to a zero-sticking signal for Ni atoms, measured by pulsing the Ni atomic beam onto a hot W foil, where no permanent sticking occurs, as described previously by our group.[46] The fraction of atoms that stick times the Ni vapor flux and pulse duration was then used to determine the number of Ni atoms per unit area that adsorbed in each pulse. This was used to scale the adsorbed heat per pulse (to get the heat per mole adsorbed) and to calculate the accumulated Ni coverage for all calorimetry and growth mode experiments.

The sticking probability of Ni on graphene/Ni(111) as a function of Ni coverage at 300 and 100 K is shown in Figure 1. The Ni coverages reported here are given in units of ML, with 1 ML defined as 1.87×10^{19} atoms/m^2, which is exactly ½ the areal density of C atoms on the

graphene surface, which grows in registry with the Ni(111) substrate, with 2 C atoms per surface Ni atom.[49–51] The results in Figure 1 show that the sticking probability at 300 K starts at 94% and increases slowly with Ni coverage, rising to a value of 97% by 4 ML. At 100 K, the sticking probability starts higher at 96% and gradually rises until reaching slightly higher than 99% by 4 ML.

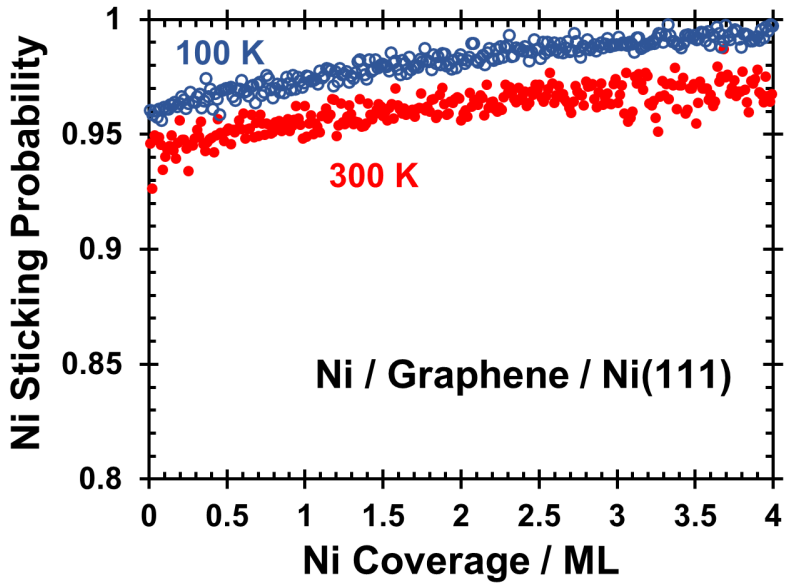

Figure 1: Sticking probability of Ni gas atoms onto graphene/Ni(111) as a function of Ni coverage at 300 K (red, filled points) and 100 K (blue, open points). The absolute coverage of 1 ML is defined here as 1.87×10^{19} atoms/m^2.

The higher sticking probability seen here at lower sample temperatures is commonly reported for metal adsorption, where it has been attributed primarily to the decreased desorption rate of diffusing metal adatoms as the temperature is decreased.[23,54] Since the ratio of the desorption rate to the diffusion rate of Ni is much smaller at 100 K when compared with 300 K, the diffusing Ni adatoms are more likely to desorb at the higher temperature before they find other Ni adatoms of Ni clusters to which they can bind.

The sticking probabilities reported here for Ni atoms deposited onto graphene/Ni(111) are up to 20% larger than those previously reported for Ag deposition on the same surface.[15] This can be attributed to a stronger binding of Ni monomers onto the graphene substrate compared with Ag monomers. This hypothesis is corroborated by previously reported DFT calculations of the adsorption energy of Ni and Ag monomers onto a graphene support, which consistently show

a much higher adsorption energy for Ni monomers when compared with Ag monomers.[55–57] The sticking probabilities measured here for Ni atoms on graphene/Ni(111) are also larger than those measured previously by our group for Ni atoms on MgO(100) at the same temperatures.[23] This also implies a stronger binding of Ni monomers to graphene than to MgO(100).

3.3 Ni Growth Morphology on Graphene/Ni(111)

The growth morphology of Ni on graphene/Ni(111) at 300 and 100 K was determined using He^+ LEIS measurements. Ni was vapor deposited onto the graphene/Ni(111) substrate in discrete amounts and the Ni LEIS signal was measured after each dose. The substrate's LEIS signal (graphitic carbon) could not be measured due to a near unity ion neutralization probability for He^+ ions scattered from graphitic carbon, as was the case for Ag deposition on graphene/Ni(111).[15,58–60] The integrated Ni LEIS signal was normalized to the signal from a thick Ni layer (>10 nm) which served as the Ni reference signal for complete coverage of the graphene surface by Ni. This normalized Ni LEIS signal then gives the fraction of the surface covered (and shadowed) by Ni particles.

The normalized Ni LEIS signals versus Ni coverage are shown in Figure 2a, along with fits of these data to different growth models for the Ni particle growth morphologies. Data shown are the averages from several repeated LEIS signal versus coverage measurements. The growth models analyzed in this study include layer-by-layer, constant height and hemispherical cap models. A layer-by-layer growth model (shown as a straight black dashed line) shows the signal that would be observed if Ni grew in a layer-by-layer fashion. As can be seen in Figure 2a, this model does not fit the data well. Instead, we found models where the Ni grows as 3D nanoparticles fit the data well. Specifically, a constant particle height model fits the 300 K data well, and a hemispherical cap model fit the 100 K data very well. These two models will be discussed in the remainder of this section. The constant height model assumes that the Ni nanoparticles have the same height at all coverages (above some tiny coverage) and have flat tops. The hemispherical cap model assumes the Ni nanoparticles have a hemispherical shape and the same average particle diameter at a given coverage, and that the number of particles per unit area is a constant, independent of coverage (above some tiny coverage).

Using the data in Figure 2a, the average Ni nanoparticle thickness can easily be calculated by converting the number of Ni atoms per m^2 to the total volume of Ni per m^2 (assuming the deposited Ni particles have the same density as bulk Ni) and dividing by the fractional area covered by Ni particles, as measured with LEIS. The average thickness is then $t = \theta \times n_{ML} \times M_{Ni} / (N_A \times \rho_{Ni} \times f)$ where θ is the total Ni coverage (in ML), n_{ML} is the Ni atomic number density that defines one monolayer ($n_{ML} = 1.87 \times 10^{19}$ atoms/m^2), M_{Ni} is the molar mass of Ni (58.69 g/mol), N_A is Avogadro's number, ρ_{Ni} is the bulk density of Ni (8.9 g/cm^3), and f is the fraction of the graphene surface area covered by Ni particles, as obtained from the He^+ LEIS measurements. The resulting average Ni particle thickness as a function of Ni coverage is shown

in Figure 2b. The thicknesses here at 100 K have been slightly corrected from the above equation by multiplying them by 1.207 to take into consideration the effect of shadowing of the support surface in LEIS near island edges, based on the hemispherical cap model (details below).

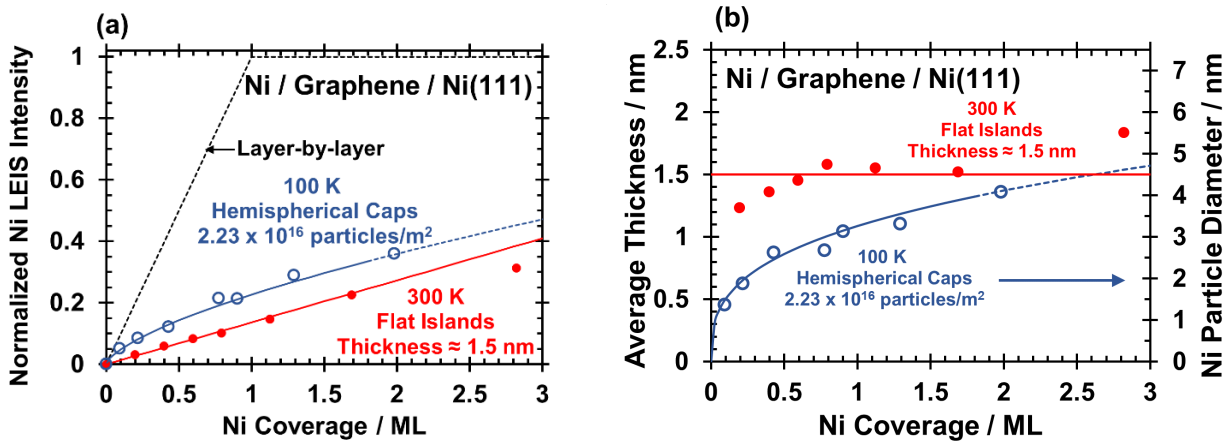

Figure 2: (a) Integrated Ni LEIS signal normalized to a thick multilayer Ni film as a function of the Ni coverage following deposition onto graphene/Ni(111) at 300 K (red, filled points) and 100 K (blue, open points). The black dashed line corresponds to the signal that would be observed if Ni grew in a layer-by-layer fashion on this substrate. The colored red line corresponds to a model in which Ni grows as flat islands with a thickness of 1.5 nm. The colored blue line corresponds to a model with Ni growing as 3D hemispherical caps with a particle density of 2.23×10^{16} particles/m^2. The dotted line above a normalized Ni LEIS signal of 0.33 is only a guide to the eye since the model should not be applied at those higher coverages. (b) Average Ni particle thickness as a function of coverage, and on the right axis, the average diameter of hemispherical caps that correspond that this thickness. The colored red line shows a constant average thickness of 1.5 nm (for 300 K) and the colored blue line corresponds to the model in which Ni grows as hemispherical caps at 100 K with a particle density of 2.23×10^{16} particles/m^2.

For the Ni growth at 300 K, the normalized Ni LEIS signal versus coverage is well-fit by a straight proportionality (red, solid line in Figure 2a). This line has a slope of 1/(7.33 ML). This proportionality indicates that at 300 K, flat Ni islands grow with an average thickness of 7.33 ML (1.5 nm), nearly independent of coverage. This model is further supported by the 300 K data in Figure 2b (red, filled points) which shows the average Ni island thickness is nearly constant with average value t = 1.54 nm. As seen, the island thickness does increase slowly with coverage.

This growth model in which Ni grows as islands with a nearly constant average height at 300 K is further supported by STM observations on the growth morphology of Ni on graphene from the literature.[36,42] Both these STM observations at room temperature clearly showed that Ni vapor deposited onto graphene forms triangular islands with flat-topped terraces. The study by

Lahiri et al. included a room temperature STM measurement of Ni on graphene/Ni(111) and showed that the islands had similar apparent heights of 1.58 ± 0.42 nm, with the flat tops being Ni(111) terraces, for a wide range of island widths (1-11 nm).[36] The study by Sicot et al. included a 300 K STM measurement of Ni on graphene/Rh(111) with an average apparent height of 1.8 nm and edge lengths between 5 to 18 nm at a Ni coverage of 0.9 ML.[42] Since the (111) face is the most stable (lowest surface energy) facet of FCC Ni, this shape provides energetic stability.

A previous study has provided a kinetics-based explanation for why particles can grow flat and keep nearly a constant (i.e., only slowly increasing) height during vapor deposition as the island diameter (or width) grows initially to be much larger than the height.[61] Such a flat shape is not the thermodynamically-preferred particle shape, but occurs instead due to kinetics. As shown in Figures 8 and 9 there,[61] when small, flat, one-atom thick islands are grown in the first layer, and if the energetics for a newly deposited adatom are appropriate, new atoms which land on top of an island will diffuse rapidly to the island edge and down-step to add instead to sites with stronger binding around the perimeter of the island. Essentially, if the top of the island is a flat Ni(111)-like surface, as shown by STM,[36] a new Ni monomer will not be stable there (since it can only make three Ni-Ni bonds there), whereas the sites around the island edges have locations where that Ni atom can make more Ni-Ni bonds than just three and thus are much more stable. Similarly, new Ni atoms which land on the support and diffuse to the island will prefer sites around the island perimeter, and not up-step to nucleate a new layer. This causes the islands to grow in diameter (or width for non-circular islands) without gaining height up to some critical diameter where diffusing Ni monomers on top of the island encounter each other and nucleate a cluster on top of the flat island, creating a nucleation site for growth of a new layer. Thereafter, individual large, flat islands grow in height in a nearly layer-by-layer fashion, and also slowly increase in width. This would lead to a collection of islands with nearly the same thickness at any given coverage (at low coverages).[61] The rate of Ni diffusion around the island edges determines whether the islands appear circular, triangular, or some other faceted shape.[62] Importantly, the small ratio of island height to width in those STM studies cited above means that it is a good approximation to neglect any shadowing effects near island edges in modelling the LEIS signal versus coverage curves at 300 K, as we have done in Figure 2.

The 100 K data is well-fit by a hemispherical cap growth model (blue line in Figure 2a and Figure 2b) first described by Diebold et al., in which all particles are assumed to have the same hemispherical shape and same average particle size at a given coverage.[63,64] These particles are also assumed in that model to have a constant areal number density at all coverages, to be consistent with classical nucleation theory in which a saturation number density is reached at a very low coverage, and thereafter the number density stays nearly constant for a large coverage range.[1,65] This model is only applied up to coverages for which $f < 33\%$, because at higher coverages the particles might begin to overlap (depending on how uniformly they are separated), so the model assumptions could break down. The regime in which the model is no longer

appropriate is illustrated in Figure 2a and Figure 2b as a dashed blue line. As shown in previous work,[64] when the particles grow as hemispherical caps the total surface area masked by the particles and their shadows is 1.207 times the metal/support interfacial area if the He^+ ion beam is incident normal to the surface and the energy analyzer detects scattered ions 45° from the surface normal, as done here. With this hemispherical cap model, the normalized Ni LEIS data can be modelled with the saturation particle density as the only fitting parameter. As shown in Figure 2a (blue solid line), the best fit to the 100 K LEIS data gives a particle density of 2.23×10^{16} particles/m^2.

For hemispherical particles, the average diameter equals three times the average thickness. This average particle diameter for this 100 K data, and its hemispherical-cap fit curve, (calculated as three times the average thickness) is shown as the right-hand axis in Figure 2b. As expected, the data for average diameter as a function of coverage also agrees well with this hemispherical cap model.

This hemispherical cap model for Ni on graphene at 100 K is somewhat different than previously reported low-temperature particle shape measurements for Ni on C(0001).[42–44] Baumer et al. studied Ni on graphite(0001) at 100 K using primarily XPS and SPA-LEED and found that the island height does not vary significantly with Ni coverage when analyzed with a flat island model.[44] However, the Ni coverages investigated in that work (<1 ML) were significantly less than those studied in the present work. Sicot et al. used STM to study 150 K Ni nanoparticles on graphene/Rh(111) and found that the particle density increased with increasing coverage while the particles remained the same size.[42] This difference from the hemispherical cap model of Figure 2 here (for graphene/Ni(111)) could be due to the fact that graphene/Rh(111) instead has a buckled Moiré pattern which creates a high-density periodic array of special sites, which may be more stable for particle nucleation, or due to the low fluxes used in that work (<10% of the flux in the present study). Marz et al.[43] used STM to study Ni deposited on HOPG(0001) at low temperatures and found dendritic Ni particles at high coverages. Their reported STM images at low coverages appear to show hemispherical Ni particles. The exact sample temperature for these experiments was unclear. (The sample was first cooled to 77 K, then transferred to a different chamber for Ni deposition, where the sample temperature could not be monitored. It seemed that the sample was quickly transferred back to the 77 K location for STM imaging.)

3.4 Heat of Adsorption of Ni on Graphene/Ni(111)

The differential heats of adsorption of Ni gas atoms onto graphene/Ni(111) as a function of Ni coverage at 300 and 100 K is shown in Figure 3. The data shows the measured heat of adsorption for a series of pulses (each with ~0.013 ML per pulse) as the Ni coverage on the sample increases. The curves shown for 300 and 100 K are averaged from several individual calorimetry runs to ensure replicability and to reduce the standard deviation in the measured

heats of adsorption. At 300 K, the initial heat of adsorption is 336 kJ/mol which then rapidly increases to 400 kJ/mol in the first 0.1 ML. Above 0.1 ML, the heat slowly increases with coverage until reaching the bulk heat of Ni sublimation (ΔH_{sub} = 430 kJ/mol) by 2 ML. At 100 K, the heat of adsorption in the first pulse is 230 kJ/mol, increases much more slowly with coverage than at 300 K, and reaches the bulk heat of Ni sublimation by 3.5 ML. As in many previous studies of the heat of metal atom adsorption for late transition metals on clean oxide single crystal surfaces[9,23,54,66,67] (and Ag adsorption on this same type of graphene surface[15]), the reason the heat increases with coverage here is that the metal atoms first nucleate very small clusters, these clusters quickly reach a constant (saturation) number density, and thereafter grow in size, so that when new metal atoms arrive, they add to larger and larger clusters as coverage increases. When a metal atom adds to a larger cluster, it typically makes more metal-metal bonds, so the heat increases. For example, when an atom adds to a trimer, it can make only three metal-metal bonds at most, whereas when it adds to a huge metal particle or extended surface, it makes six metal-metal bonds (on average) for FCC or HCP packing. (Atoms in the bulk of both these structures have 12 nearest neighbors, so that a nearest-neighbor bond additivity model predicts that the sublimation energy equals 12/2 = 6 times the nearest-neighbor bond energy, which also equals an atom's adsorption energy on a kink site at the surface.)

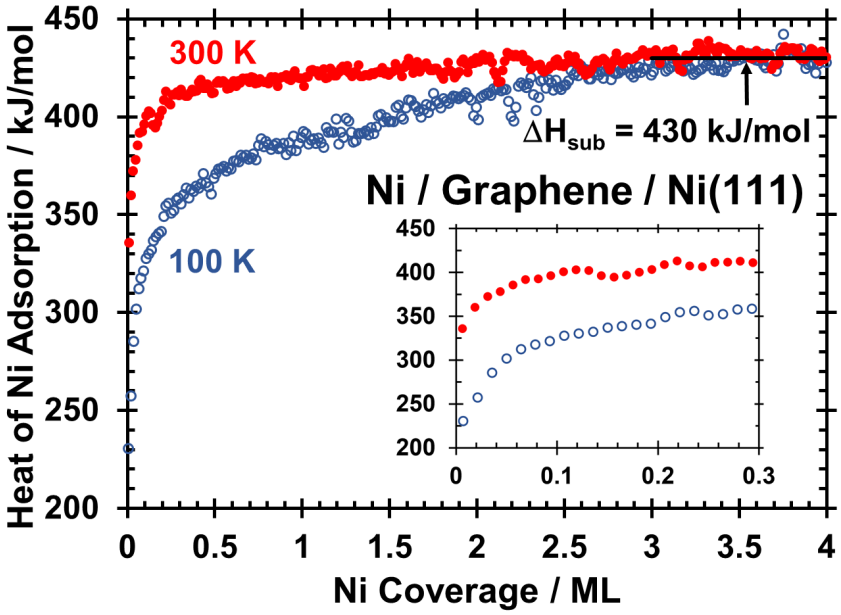

Figure 3: Differential heat of adsorption of Ni gas atoms onto graphene/Ni(111) as a function of Ni coverage at 300 K (red, filled points) and 100 K (blue, open points). The inset shows the low coverage regime (<0.3 ML) on an expanded scale.

The lower initial heat of adsorption and slower increase in the heats of adsorption at 100 K compared with 300 K is attributed primarily to Ni particle size differences between the two temperatures. At any given coverage below 2 ML, the Ni particles at 100 K are much smaller than at 300 K. For example, one STM study mentioned above showed at 0.9 ML an average flat-topped particle height of ~1.8 nm and width of ~12 nm at 300 K.[42] At this coverage for 100 K, the particle diameter in only ~3 nm (based on the hemispherical cap model fit in Figure 2). These tiny hemispherical caps formed at 100 K have a much larger fraction of undercoordinated atoms (i.e., atoms with fewer Ni-Ni bonds and thus which are less stable) in comparison to the larger, faceted particles formed at 300 K. Similarly, when a newly-deposited Ni adatom diffuses to and binds to a small hemispherical cap, there is a much greater chance that it attaches to a site where it is highly undercoordinated (i.e., where that new adatom forms fewer Ni-Ni bonds than at 300 K). For the larger particles at 300 K, there are sites where a new Ni adatom can make more Ni-Ni bonds, and the new Ni adatom can diffuse fast enough to find those stronger-binding sites. For example, when an adatom adds to a trimer, it can only make 3 Ni-Ni bonds, whereas when it adds to a very large particle at 300 K, it can make 6 Ni-Ni bonds at a kink site on a Ni(111) facet's step edge. In the large particle size limit, each added Ni atom also makes 6 Ni-Ni bonds and has a differential heat of adsorption equal to the bulk heat of sublimation. (In a simple nearest neighbor bond-additivity model, the bulk sublimation energy or cohesive energy equals 6 times the Ni-Ni bond energy, since atoms in the bulk have 12 nearest neighbors and each of these 12 bonds is shared by 2 atoms: 12/2 = 6. This is twice the total Ni-Ni bond energy gained when instead Ni adds to a trimer.) Consequently, fewer Ni-Ni bonds on average are formed when a Ni atom attaches to a particle at 100 K when compared to 300 K at the same coverage, and the measured heats of adsorption are smaller. This continues until the hemispherical caps grow sufficiently large that they are dominated by sites where new Ni atoms can make as many Ni-Ni bonds upon adsorption as at 300 K (~3.5 ML of Ni coverage). This increase in adsorption energy with coverage as more Ni-Ni bonds are made is mitigated to some extent by the fact that more of the Ni atoms in smaller particles also bond to the underlying graphene, as quantified below via the adhesion energy at this Ni / graphene interface.

Using the average particle diameter as a function of coverage from Figure 2b allows us to replot the 100 K heats of adsorption versus coverage from Figure 3 in the form of heats of adsorption versus the effective Ni particle diameter to which the new Ni atoms add, as shown in Figure 4a. This procedure was not possible for the 300 K heats of adsorption since our constant height model does not allow for the determination of the Ni particle density nor their average lateral dimensions. From Figure 4a, we can see again that the heats of adsorption at 100 K increase rapidly with particle size due to the deposited atoms forming more Ni-Ni bonds as the particle size increases, as described above.

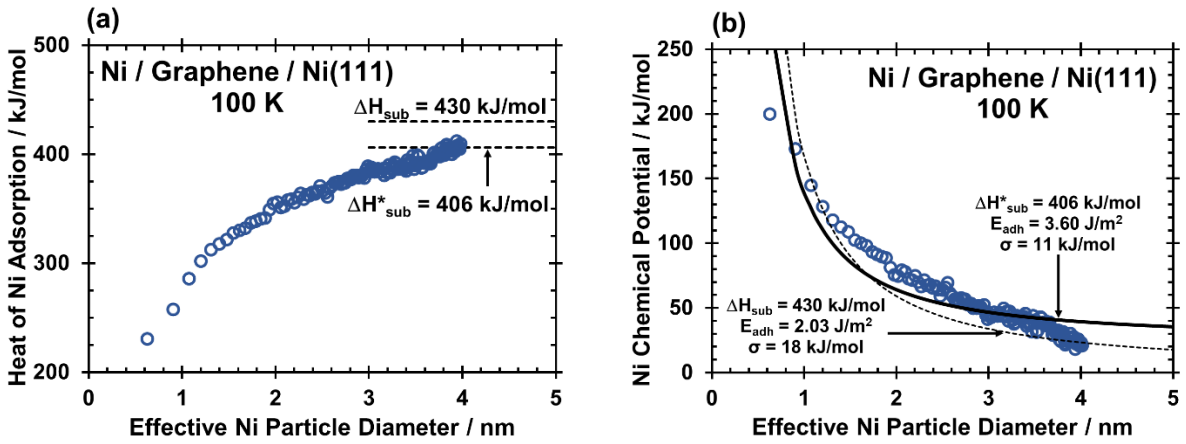

Figure 4: (a) Differential heat of adsorption of Ni vapor adsorption onto graphene/Ni(111) at 100 K as a function of the effective Ni particle diameter to which Ni adds during growth. Particles with diameters larger than 4 nm could not be analyzed since the hemispherical cap model assumptions break down above that size. (b) Chemical potential of Ni atoms on graphene/Ni(111) at 100 K as a function of the average Ni particle diameter to which Ni atoms add during growth.

3.5 Chemical Potential and Adhesion of Ni on Graphene/Ni(111)

If we assume the size-dependent changes in the entropic contributions to the free energy are negligible compared to the very large enthalpic contributions for this system, we can calculate the chemical potential of Ni atoms in nanoparticles on graphene/Ni(111) at each size. The chemical potential relative to that of bulk Ni is simply the difference between the heat of sublimation and the measured differential heat of Ni adsorption at that size. The resulting Ni chemical potential as a function of the effective Ni particle diameter is shown in Figure 4b. As can be seen, the Ni chemical potential begins high (200 kJ/mol) and rapidly decreases with the particle diameter. Similar behavior has been shown for nanoparticles in this size range for many transition metals on oxides and Ag on graphene.[2]

Previous work studying metal nanoparticles supported on single crystal oxides has shown that the chemical potential for hemispherical nanoparticles is well approximated by[2,8]

$$\mu(D) = \left(3\gamma_{v/m} - E_{adh}\right)\left(1 + \frac{D_0}{D}\right)\left(\frac{2V_m}{D}\right) \quad (1)$$

where $\gamma_{v/m}$ is the surface free energy of the bulk metal (2.38 J/m^2 for Ni), E_{adh} is the adhesion energy of the metal/support (Ni/graphene here) interface, V_m is the molar volume of the supported metal (6.59 m^3/mol for Ni), and $(1 + D_0/D)$ with D_0 = 1.5 nm is an empirical factor that was added to the equation as originally derived (assuming that $\gamma_{v/m}$ and E_{adh} are independent of size[10]) and has been shown to account for the increase in $\gamma_{v/m}$ and E_{adh} (relative

to their bulk values) as the supported nanoparticles decrease in size for many different metals and oxide supports.[2,8] This equation has also been shown to fit data for Ag on graphene/Ni(111) very well.[15] Using eq 1, E_{adh} is the only unknown variable which provides a method to calculate E_{adh} by fitting the measured Ni chemical potential as a function of the diameter.

The heat of adsorption here does not reach the bulk heat of Ni sublimation at the largest particle sizes analyzed (~4 nm), in contrast to many other metal on support systems studied with SCAC and He^+ LEIS[15,54,66,67]. This same phenomenon has been observed for both systems involving Ni deposition studied previously by our group, namely Ni/MgO(100) and Ni/CeO_2(111), and was attributed to a structural phase change whereby Ni adopts hexagon close packed (HCP) structure for very small Ni particles (<5 nm) but takes on the usual face-centered cubic (FCC) structure for large particles.[8,23]

As discussed in previous work from our group,[8] eq 1 can be modified to account for this difference in crystal packing, which results in the following equation:

$$\mu(D) = \left(3\gamma_{v/m} - E_{adh}\right)\left(1 + \frac{D_0}{D}\right)\left(\frac{2V_m}{D}\right) + (\Delta H_{sub} - \Delta H^*_{sub}) \quad (2)$$

where ΔH^*_{sub} is the heat of sublimation of the small-particle HCP phase (in the large-size limit) and ΔH_{sub} is the bulk FCC phase heat of sublimation (430 kJ/mol for Ni). Eq 2 now has two parameters, E_{adh} and ΔH^*_{sub}, that are required to fit the experimental data.

Both eq 1 and eq 2 were used to fit the measured chemical potential data and these fits are shown as dotted and solid lines (respectively) in Figure 4b. Using eq 1 to fit the data gave a best-fit value for E_{adh} = 2.03 J/m^2 and the fit had a standard deviation (σ) of 18 kJ/mol relative to the measured values, while using eq 2 gave best-fit values of E_{adh} = 3.60 J/m^2 and ΔH^*_{sub} = 406 kJ/mol, and had a standard deviation of 11 kJ/mol versus measured values.

These standard deviations show that using eq 2 gives a better fit to the measured chemical potentials versus size, suggesting the formation of a different phase (HCP) for small Ni nanoparticles supported on graphene/Ni(111) than for large Ni particles (which prefer the bulk FCC phase). For Ni/MgO(100), a best-fit value of ΔH^*_{sub} = 405 kJ/mol was determined with the same method,[23] while Ni/CeO_{2-x}(111) gave a best-fit value of ΔH^*_{sub} = 404 kJ/mol.[8] The best-fit value of ΔH^*_{sub} is almost identical for all three of these systems, suggesting that very small, supported Ni nanoparticles often form the same HCP phase.

Hexagonal close packed Ni films and nanoparticles have been observed on MgO(100), Au(100), and Ru(11$\bar{2}$0), Ru(1$\bar{1}$00), and carbon nanotubes and the formation of this HCP phase has been attributed to size, lattice strain, and energetic effects.[68–72] This HCP Ni phase has also been reported for small unsupported Ni nanoparticles using a variety of different preparation methods where the HCP Ni phase can be stabilized by surface decoration by ligands.[73–75] This HCP phase will only form for metals in which the FCC structure is only very slightly more stable than the HCP structure and differential size effects can change the lattice packing. Indeed, it was

found that the HCP structure for Ni nanoparticles on MgO(100) and CeO_2(111) had a heat of sublimation that was only 25 to 26 kJ/mol smaller than that for FCC Ni.[8,23] In addition, DFT calculations found that the HCP phase is only slightly less stable in the bulk than the normal FCC phase, but the surface energy per unit area of the HCP phase is lower than the surface energy of the FCC phase.[76] This surface energy difference could cause the HCP phase to be more stable than the FCC phase below some critical particle size. When the surface to volume ratio decreases as the nanoparticles grow, the HCP then transforms to the FCC phase, well known to be the most stable phase for very large particles.

In much of the previous work studying the HCP Ni phase, it has been argued that the HCP phase is caused by lattice strain.[8,23,68,70,71] However, in this present study, the C(0001) (graphene/Ni(111)) substrate is almost perfectly lattice matched with bulk FCC Ni(111) and lattice strain is not expected in the large size limit (although there may be lattice strain for small Ni particles, since small metal nanoparticles are well known to contract slightly in lattice constant relative to bulk metal). The Ni clusters formed on graphene here could nucleate from a HCP-like cluster structure and/or be thermodynamically stabilized due to the lower surface energy of the HCP phase mentioned above. In addition to this affect, a carbon environment also facilitates the stabilization of the Ni HCP phase. This has been found in the thermal decomposition of Ni_3C nanoparticles and PVD growth of Ni on carbon nanotubes were stabilized by a carbon shell around the Ni particles.[72,77] Here we do not observe any evidence of Ni particle encapsulation with our LEIS and SCAC experiments. However, a large fraction of the surface Ni atoms in the small nanoparticles are in contact with carbon support surface, giving rise to a similar effect.

The continued decrease in Ni chemical potential as the particles grow beyond a diameter of 3.5 nm suggests that the Ni particles may transition from the HCP phase to the thermodynamically stable FCC phase near this particle size. If we fix the value of ΔH^*_{sub} = 404.5 kJ/mol (the average of the values for Ni/MgO(100) and Ni/CeO_{2-x}(111)) and fit the chemical potential with eq 2 only up to a diameter of 3.5 nm, we instead obtain a best-fit value of E_{adh} = 3.53 J/m^2 with a standard deviation of 8.7 kJ/mol relative to measured values, in close agreement with the values calculated above.

There is no previously reported direct evidence for the HCP phase for small Ni particles on graphene. We have only postulated it here to better explain how the heat of Ni adsorption varies with coverage at 100 K, specifically the continued increase at very high coverages (large particle sizes) when the Ni is proposed here to transition from HCP to the more stable FCC phase.

4. Discussion

The adhesion energy of 3.60 J/m^2 found here for Ni on graphene/Ni(111) can be directly compared with the work of Lahiri et al. in which room temperature STM measurements of Ni nanoparticles on graphene/Ni(111) were used along with the Wulff construction to determine the adhesion energy for this same system.[36] Their results showed an adhesion energy of 3.5 J/m^2 in the large particle size limit (for Ni that we expect was in the FCC structure), within 3% of our value measured by calorimetry here at 100 K for HCP particles (extrapolated to the large-size limit). Despite this FCC versus HCP structural difference, this close agreement supports the conclusion that eq 2 is appropriate for analyzing the chemical potential data in Figure 4b. These values are also consistent with DFT calculations done in that same work,[36] which found an adhesion energy of 3.47 J/m^2 for a Ni adlayer on graphene/Ni(111). Those same DFT calculations surprisingly found an adhesion energy of only 0.81 J/m^2 at the graphene/Ni(111) interface. They attributed this large increase in interfacial bonding for Ni/graphene/Ni(111) to an increase in electronic density at the interface due to the underlying Ni(111) substrate, compared to Ni on free-standing, pristine graphene.

An adhesion energy of 3.6 J/m^2 implies a contact angle (θ) of 58˚ for a spherical cap ($1 + \cos\theta = E_{adh} / \gamma_{v/m}$),[78] whereas the hemispherical cap structure assumed above has 90˚ contact angle (which would occur only if $E_{adh} = \gamma_{v/m}$ = 2.38 J/m^2). Thus, there is clearly some error in the adhesion energy estimated here. We are developing a method that can analyze the combination of LEIS data on average particle thickness and calorimetric chemical potential versus coverage for spherical caps with arbitrary contact angle, but that requires rather complex theoretical development that will take many more months to complete.

This adhesion energy of 3.60 J/m^2 from eq 2 can further be compared with the adhesion energy of 1.80 J/m^2 for Ag on graphene/Ni(111).[15] This stronger adhesion energy of Ni compared with Ag is consistent with DFT calculations which show a stronger binding strength of Ni monomers to graphene.[55–57] In comparison to Ni on oxide supports, Ni/graphene has an intermediate adhesion energy between Ni/MgO(100) and Ni/CeO_2(111), which have adhesion energies of 3.05 J/m^2 and 4.39 J/m^2 respectively.[8,23]

This intermediate adhesion energy for Ni on graphene/Ni(111) has important implications for the design of heterogeneous catalysts. As seen in eq 2, this intermediate adhesion energy means that for a given particle size (below ~6 nm) the Ni chemical potential on (metal-supported) graphene will be somewhat higher than Ni on CeO_{2-x}(111) but lower than Ni on MgO(100). Given the quantitative relationship that shows that a high chemical potential leads to higher sintering rates,[9,79,80] we expect that the rate of catalyst deactivation by sintering will be lower for Ni supported on metal-supported graphene compared with MgO, but higher than for Ni supported on CeO_2. In addition, many qualitative predictions have shown that metal nanoparticles with a higher chemical potential will bind small, adsorbed intermediates more strongly.[2,8,9] This suggests that nanoparticles supported on metal-supported graphene will bind

adsorbed intermediates more strongly than particles of the same size supported on CeO_2, but less strongly than those particles supported on MgO.

Our measured heats of adsorption can also be compared with DFT calculations in the literature. If we assume the smallest particles measured at 100 K have a hemispherical geometry and the same density as bulk Ni (8.90 g/cm^3), we can determine that these smallest particles have an average of 13 atoms with a heat of adsorption of 230 kJ/mol. This heat of Ni adsorption for making Ni_{13} on graphene/Ni(111) can be compared with DFT calculations that found a Ni gas atom adsorption energy of 2.66 – 3.02 eV/atom (262-298 kJ/mol) to form 3-dimensional Ni cluster sizes of 4 to 10 atoms bound to the surface of pristine, free-standing graphene.[38–41] While similar to our experimental measurement of 230 kJ/mol, these DFT calculations all found a 32 to 68 kJ per mol Ni stronger binding of 3D Ni clusters to free-standing graphene than we measure for 3D Ni_{13} on graphene/Ni(111).

This difference between the measured Ni_{13} binding enthalpy of 230 kJ/mol and the calculated Ni_4-Ni_{10} binding energies of 262-298 kJ/mol could be explained by the stabilization of the graphene film by the Ni(111) substrate used in our experiments. If we assume the graphene/Ni(111) adhesion energy is the same E_{adh} as measured above (3.6 J/m^2), we can convert this adhesion energy to ~116 kJ per mol surface Ni atoms using the Ni(111) surface atom density (1.87×10^{19} atoms/m^2) and Avogadro's number. This corresponds to 58 kJ per mol surface C atoms, since there are two C atoms for every Ni surface atom in this graphene film (see above). Thus, the C atoms in this graphene on Ni(111) film are stabilized by ~58 kJ/mol when bound to Ni(111) compared with free-standing graphene. This can partly explain why our measured adsorption enthalpy of making Ni_{13} on graphene/Ni(111) is significantly smaller than DFT results for making Ni_4-Ni_{10} on free-standing graphene despite the larger cohesive energy contribution expected for the larger particle size we measured.

The differences in growth modes and particle sizes between 300 K and 100 K are mainly due to the differences in the diffusion rate of Ni monomers. It is well-known that the number density of islands is typically much larger at 100 K than 300 K during metal vapor deposition.[1,9] The rapid down-stepping that enables the growth of wide, flat-topped islands at 300 K is not expected to occur at 100 K. Thus, the particles will be much smaller at 100 K than 300 K causing a much higher surface area / volume ratio. For these small Ni nanoparticles, the DFT-predicted lower surface energy of the HCP phase compared with the FCC phase[76] might dominate over the small bulk energy difference between these two phases and might cause these small nanoparticles to assume the HCP phase at 100 K, whereas at the same coverage the particles are much larger at 300 K and are more likely to assume the bulk FCC phase at 300 K. This difference in phase might also contribute to the difference in island shape between 100 K and 300 K.

5. Conclusions

Calorimetric adsorption energies of Ni vapor deposited onto graphene/Ni(111) are used in conjunction with the growth morphology to determine the Ni chemical potential as a function of Ni nanoparticle size as well as the adhesion energy of Ni metal to graphene/Ni(111). The He^+ LEIS experiments showed that Ni grows as 3D nanoparticles on graphene/Ni(111) at 100 K with a particle density of 2.23×10^{16} particles/m^2. At 300 K, Ni vapor deposited onto graphene/Ni(111) instead forms flat-topped islands with an average height of 1.54 nm in the coverage range 0.2 to 3.0 ML. QMS measurements showed an initial sticking probability for Ni vapor of 94% at 300 K and 96% at 100 K. This is consistent with expectations since the ratio of the desorption rate to the diffusion rate is much lower at 100 K than at 300 K (since the activation barrier for desorption is much larger than that for diffusion). The heat of Ni adsorption at 300 K is initially 336 kJ/mol and rapidly increases to 400 kJ/mol in the first 0.1 ML of Ni deposition (where the Ni particles already reach ~1 nm thick), and further increases to the bulk heat of Ni sublimation (430 kJ/mol) by 2 ML. The heat of adsorption at 100 K begins at 230 kJ/mol, increases much more slowly with coverage than at 300 K, and reaches the bulk heat of Ni sublimation by 3.5 ML. The Ni chemical potential as a function of average Ni particle diameter (from 0.5 to 4 nm) was determined from the 100 K heats of adsorption and was shown to decrease with Ni coverage and diameter. By fitting the measured chemical potential as a function of diameter to a previously reported model, we determined an adhesion energy of 3.6 J/m^2 for Ni particles (in the larger-size limit) on graphene/Ni(111). This adhesion energy is in good agreement with STM and DFT investigations of Ni/graphene/Ni(111) and its value is in between those for Ni/MgO(100) and Ni/CeO_2(111). These chemical potential versus diameter results are best fitted if we assume that these small Ni nanoparticles at 100 K form an HCP phase with a sublimation enthalpy ~25 kJ/mol smaller than that of the normal bulk FCC phase, consistent with those earlier reports for Ni on MgO(100) and CeO_2(111).

6. Acknowledgements

The authors acknowledge the Department of Energy, Office of Basic Energy Sciences, under Grant Number DE-FG02-96ER14630, for support of this work.

7. References

1. C. T. Campbell. Ultrathin metal films and particles on oxide surfaces: structural, electronic and chemisorptive properties. *Surf. Sci. Rep.* **27**, 1–111 (1997).

2. C. T. Campbell & Z. Mao. Chemical Potential of Metal Atoms in Supported Nanoparticles: Dependence upon Particle Size and Support. *ACS Catal.* **7**, 8460-8466. See also erratum: DOI: 10.1021/acscatal (2017).

3. D. R. Rainer & D. W. Goodman. Metal Clusters on Ultrathin Oxide Films: Model

Catalysts for Surface Science Studies. *J. Mol. Catal. A Chem.* **131**, 259 (1998).

4. L. T. Roling, L. Li, & F. Abild-Pedersen. Configurational Energies of Nanoparticles Based on Metal-Metal Coordination. *J. Phys. Chem. C* **121**, 23002–23010 (2017).

5. M. P. Andersson, F. Abild-Pedersen, I. N. Remediakis, T. Bligaard, G. Jones, J. Engbæk, O. Lytken, S. Horch, J. H. Nielsen, J. Sehested, J. R. Rostrup-Nielsen, J. K. Nørskov, & I. Chorkendorff. Structure sensitivity of the methanation reaction: H2-induced CO dissociation on nickel surfaces. *J. Catal.* **255**, 6–19 (2008).

6. H. Tsunoyama, H. Sakurai, Y. Negishi, & T. Tsukuda. Size-specific catalytic activity of polymer-stabilized gold nanoclusters for aerobic alcohol oxidation in water. *J. Am. Chem. Soc.* **127**, 9374–9375 (2005).

7. M. Shao, A. Peles, & K. Shoemaker. Electrocatalysis on platinum nanoparticles: Particle size effect on oxygen reduction reaction activity. *Nano Lett.* **11**, 3714–3719 (2011).

8. Z. Mao & C. T. Campbell. Predicting a Key Catalyst-Performance Descriptor for Supported Metal Nanoparticles: Metal Chemical Potential. *ACS Catal.* **11**, 8284-8291. See also erratum: DOI: 10.1021/acscatal (2021).

9. C. T. Campbell & J. R. V. Sellers. Anchored metal nanoparticles: Effects of support and size on their energy, sintering resistance and reactivity. *Faraday Discussions* **162**, 9–30 (2013).

10. S. L. Hemmingson & C. T. Campbell. Trends in Adhesion Energies of Metal Nanoparticles on Oxide Surfaces: Understanding Support Effects in Catalysis and Nanotechnology. *ACS Nano* **11**, 1196–1203 (2017).

11. X. Liu & L. Dai. Carbon-based metal-free catalysts. *Nature Reviews Materials* **1**, 16064 (2016).

12. X. Duan, J. Xu, Z. Wei, J. Ma, S. Guo, S. Wang, H. Liu, & S. Dou. Metal-Free Carbon Materials for CO2 Electrochemical Reduction. *Adv. Mater.* **29**, 1701784 (2017).

13. I. C. Gerber & P. Serp. A Theory/Experience Description of Support Effects in Carbon-Supported Catalysts. *Chemical Reviews* **120**, 1250–1349 (2020).

14. E. Lam & J. H. T. Luong. Carbon Materials as Catalyst Supports and Catalysts in the Transformation of Biomass to Fuels and Chemicals. *ACS Catal.* **4**, 3393–3410 (2014).

15. J. R. Rumptz, Z. Mao, & C. T. Campbell. Size-Dependent Adsorption and Adhesion Energetics of Ag Nanoparticles on Graphene Films on Ni(111) by Calorimetry. *ACS Catal.* **12**, 2888–2897 (2022).

16. J. Guo, H. Lou, H. Zhao, D. Chai, & X. Zheng. Dry reforming of methane over nickel catalysts supported on magnesium aluminate spinels. *Appl. Catal. A* **273**, 75–82 (2004).

17. J. A. Montoya, E. Romero-Pascual, C. Gimon, P. Del Angel, & A. Monzon. Methane reforming with CO2 over Ni/ZrO2–CeO2 catalysts prepared by sol–gel. *Catal. Today* **63**, 71–85 (2000).

18. S. Li & J. Gong. Strategies for improving the performance and stability of Ni-based

catalysts for reforming reactions. *Chem. Soc. Rev.* **43**, 7245–7256 (2014).

19. D. Li, Y. Nakagawa, & K. Tomishige. Methane reforming to synthesis gas over Ni catalysts modified with noble metals. *Appl. Catal. A* **408**, 1–24 (2011).

20. W. Q. Xu, Z. Y. Liu, A. C. Johnston-Peck, S. D. Senanayake, G. Zhou, D. Stacchiola, E. A. Stach, & J. A. Rodriguez. Steam reforming of ethanol on Ni/CeO2: Reaction pathway and interaction between Ni and the CeO2support. *ACS Catal.* **3**, 975–984 (2013).

21. S. D. Senanayake, J. Evans, S. Agnoli, L. Barrio, T. L. Chen, J. Hrbek, & J. A. Rodriguez. Water-gas shift and CO methanation reactions over Ni-CeO2(111) catalysts. in *Topics in Catalysis* **54**, 34–41 (Springer, 2011).

22. Z. Mao, P. G. Lustemberg, J. R. Rumptz, M. V. Ganduglia-Pirovano, & C. T. Campbell. Ni Nanoparticles on CeO2(111): Energetics, Electron Transfer, and Structure by Ni Adsorption Calorimetry, Spectroscopies, and Density Functional Theory. *ACS Catal.* **10**, 5101–5114 (2020).

23. Z. Mao, W. Zhao, Z. A. Al-Mualem, & C. T. Campbell. Energetics and Structure of Nickel Atoms and Nanoparticles on MgO(100). *J. Phys. Chem. C* **124**, 14685–14695 (2020).

24. C. Vogt, E. Groeneveld, G. Kamsma, M. Nachtegaal, L. Lu, C. J. Kiely, P. H. Berben, F. Meirer, & B. M. Weckhuysen. Unravelling structure sensitivity in CO2 hydrogenation over nickel. *Nat. Catal.* **1**, 127–134 (2018).

25. C. Vogt, M. Monai, E. B. Sterk, J. Palle, A. E. M. Melcherts, B. Zijlstra, E. Groeneveld, P. H. Berben, J. M. Boereboom, E. J. M. Hensen, F. Meirer, I. A. W. Filot, & B. M. Weckhuysen. Understanding carbon dioxide activation and carbon-carbon coupling over nickel. *Nat. Commun.* **10**, 1–10 (2019).

26. G. S. Ferdowsi, S. A. Seyedsadjadi, & A. Ghaffarinejad. Ni nanoparticle modified graphite electrode for methanol electrocatalytic oxidation in alkaline media. *J. Nanostructure Chem.* **5**, 17–23 (2015).

27. A. B. Soliman, H. S. Abdel-Samad, S. S. Abdel Rehim, M. A. Ahmed, & H. H. Hassan. High performance nano-Ni/Graphite electrode for electro-oxidation in direct alkaline ethanol fuel cells. *J. Power Sources* **325**, 653–663 (2016).

28. B. M. Thamer, M. H. El-Newehy, N. A. M. Barakat, M. A. Abdelkareem, S. S. Al-Deyab, & H. Y. Kim. In-situ synthesis of Ni/N-doped CNFs-supported graphite disk as effective immobilized catalyst for methanol electrooxidation. *Int. J. Hydrogen Energy* **40**, 14845–14856 (2015).

29. Z. Zhuang, S. A. Giles, J. Zheng, G. R. Jenness, S. Caratzoulas, D. G. Vlachos, & Y. Yan. Nickel supported on nitrogen-doped carbon nanotubes as hydrogen oxidation reaction catalyst in alkaline electrolyte. *Nat. Commun.* **7**, 1–8 (2016).

30. G. R. Dieckmann & S. H. Langer. Comparisons of Ebonex® and graphite supports for platinum and nickel electrocatalysts. *Electrochim. Acta* **44**, 437–444 (1998).

31. Y. J. Wang, N. Zhao, B. Fang, H. Li, X. T. Bi, & H. Wang. Carbon-Supported Pt-Based

Alloy Electrocatalysts for the Oxygen Reduction Reaction in Polymer Electrolyte Membrane Fuel Cells: Particle Size, Shape, and Composition Manipulation and Their Impact to Activity. *Chemical Reviews* **115**, 3433–3467 (2015).

32. U. Sanyal, Y. Song, N. Singh, J. L. Fulton, J. Herranz, A. Jentys, O. Y. Gutiérrez, & J. A. Lercher. Structure Sensitivity in Hydrogenation Reactions on Pt/C in Aqueous-phase. *ChemCatChem* **11**, 575–582 (2019).

33. N. Singh, U. Sanyal, G. Ruehl, K. A. Stoerzinger, O. Y. Gutiérrez, D. M. Camaioni, J. L. Fulton, J. A. Lercher, & C. T. Campbell. Aqueous phase catalytic and electrocatalytic hydrogenation of phenol and benzaldehyde over platinum group metals. *J. Catal.* **382**, 372–384 (2020).

34. S. Mukerjee. Particle size and structural effects in platinum electrocatalysis. *Journal of Applied Electrochemistry* **20**, 537–548 (1990).

35. S. Mukerjee & J. McBreen. Effect of particle size on the electrocatalysis by carbon-supported Pt electrocatalysts: An in situ XAS investigation. *J. Electroanal. Chem.* **448**, 163–171 (1998).

36. J. Lahiri, T. S. Miller, A. J. Ross, L. Adamska, I. I. Oleynik, & M. Batzill. Graphene growth and stability at nickel surfaces. *New J. Phys.* **13**, 025001 (2011).

37. D. Appy, H. Lei, C. Z. Wang, M. C. Tringides, D. J. Liu, J. W. Evans, & P. A. Thiel. Transition metals on the (0001) surface of graphite: Fundamental aspects of adsorption, diffusion, and morphology. *Progress in Surface Science* **89**, 219–238 (2014).

38. R. E. Ambrusi, V. Orazi, J. M. Marchetti, & M. E. Pronsato. Ni clusters embedded in multivacancy graphene substrates. *J. Phys. Chem. Solids* **138**, 109258 (2020).

39. X. Zhou, W. Chu, W. Sun, Y. Zhou, & Y. Xue. Enhanced interaction of nickel clusters with pyridinic-N (B) doped graphene using DFT simulation. *Comput. Theor. Chem.* **1120**, 8–16 (2017).

40. W. Gao, J. E. Mueller, J. Anton, Q. Jiang, & T. Jacob. Nickel cluster growth on defect sites of graphene: A computational study. *Angew. Chemie - Int. Ed.* **52**, 14237–14241 (2013).

41. C. R. C. Rêgo, P. Tereshchuk, L. N. Oliveira, & J. L. F. Da Silva. Graphene-supported small transition-metal clusters: A density functional theory investigation within van der Waals corrections. *Phys. Rev. B* **95**, 235422 (2017).

42. M. Sicot, S. Bouvron, O. Zander, U. Rüdiger, Y. S. Dedkov, & M. Fonin. Nucleation and growth of nickel nanoclusters on graphene Moiŕ on Rh(111). *Appl. Phys. Lett.* **96**, 93115 (2010).

43. M. Marz, K. Sagisaka, & D. Fujita. Ni nanocrystals on hopg(0001): A scanning tunnelling microscope study. *Beilstein J. Nanotechnol.* **4**, 406–417 (2013).

44. M. Bäumer, J. Libuda, & H. J. Freund. The temperature dependent growth mode of nickel on the basal plane of graphite. *Surf. Sci.* **327**, 321–329 (1995).

45. J. R. V Sellers, T. E. James, S. L. Hemmingson, J. A. Farmer, & C. T. Campbell. Adsorption calorimetry during metal vapor deposition on single crystal surfaces: Increased flux, reduced optical radiation, and real-time flux and reflectivity measurements. in *Review of Scientific Instruments* **84**, 123901–123901 (2013).

46. J. T. Stuckless, N. A. Frei, & C. T. Campbell. A novel single-crystal adsorption calorimeter and additions for determining metal adsorption and adhesion energies. *Rev. Sci. Instrum.* **69**, 2427–2438 (1998).

47. D. A. King & M. G. Wells. Reaction mechanism in chemisorption kinetics: nitrogen on the {100} plane of tungsten. *Proc. R. Soc. London. A. Math. Phys. Sci.* **339**, 245–269 (1974).

48. M. Batzill. The surface science of graphene: Metal interfaces, CVD synthesis, nanoribbons, chemical modifications, and defects. *Surface Science Reports* **67**, 83–115 (2012).

49. J. Wintterlin & M. L. Bocquet. Graphene on metal surfaces. *Surf. Sci.* **603**, 1841–1852 (2009).

50. A. Dahal & M. Batzill. Graphene–nickel interfaces: a review. *Nanoscale* **6**, 2548–2562 (2014).

51. W. Zhao, S. M. Kozlov, O. Höfert, K. Gotterbarm, M. P. A. Lorenz, F. Viñes, C. Papp, A. Görling, & H. P. Steinrück. Graphene on Ni(111): Coexistence of different surface structures. *J. Phys. Chem. Lett.* **2**, 759–764 (2011).

52. D. W. Goodman, R. D. Kelley, T. E. Madey, & J. T. Yates. Kinetics of the hydrogenation of CO over a single crystal nickel catalyst. *J. Catal.* **63**, 226–234 (1980).

53. J. P. Coad & J. C. Rivière. Auger spectroscopy of carbon on nickel. *Surf. Sci.* **25**, 609–624 (1971).

54. S. L. Hemmingson, G. M. Feeley, N. J. Miyake, & C. T. Campbell. Energetics of 2D and 3D Gold Nanoparticles on MgO(100): Influence of Particle Size and Defects on Gold Adsorption and Adhesion Energies. *ACS Catal.* **7**, 2151–2163 (2017).

55. X. Liu, Y. Han, J. W. Evans, A. K. Engstfeld, R. J. Behm, M. C. Tringides, M. Hupalo, H. Q. Lin, L. Huang, K. M. Ho, D. Appy, P. A. Thiel, & C. Z. Wang. Growth morphology and properties of metals on graphene. *Progress in Surface Science* **90**, 397–443 (2015).

56. M. Manadé, F. Viñes, & F. Illas. Transition metal adatoms on graphene: A systematic density functional study. *Carbon N. Y.* **95**, 525–534 (2015).

57. O. V Yazyev & A. Pasquarello. Metal adatoms on graphene and hexagonal boron nitride: Towards rational design of self-assembly templates. *Phys. Rev. B - Condens. Matter Mater. Phys.* **82**, 045407 (2010).

58. S. N. Mikhailov, L. C. A. van den Oetelaar, & H. H. Brongersma. Strong matrix effect in low-energy He+ ion scattering from carbon. *Nucl. Inst. Methods Phys. Res. B* **93**, 210–214 (1994).

59. L. C. A. van den Oetelaar, S. N. Mikhailov, & H. H. Brongersma. Mechanism of neutralization in low-energy He+ ion scattering from carbidic and graphitic carbon species on rhenium. *Nucl. Inst. Methods Phys. Res. B* **85**, 420–423 (1994).

60. N. B. Luna, F. J. Bonetto, R. A. Vidal, E. C. Goldberg, & J. Ferrón. Low energy ion scattering in He/HOPG system. *J. Mol. Catal. A Chem.* **281**, 237–240 (2008).

61. K. H. Ernst, A. Ludviksson, R. Zhang, J. Yoshihara, & C. T. Campbell. Growth model for metal films on oxide surfaces: Cu on ZnO (0001)-O. *Phys. Rev. B* **47**, 13782 (1993).

62. E. Soy, N. P. Guisinger, & M. Trenary. Growth of Pd Nanoclusters on Single-Layer Graphene on Cu(111). *J. Phys. Chem. B* **122**, 572–577 (2018).

63. U. Diebold, J. M. Pan, & T. E. L. B.-M. on T. then (110) Madey. Growth Mode of Ultrathin Copper Overlayers on TiO2(110). *Phys. Rev. B* **47**, 3868–3876 (1993).

64. C. T. Campbell & T. E. James. Ion scattering spectroscopy intensities for supported nanoparticles: The hemispherical cap model. *Surf. Sci.* **641**, 166–169 (2015).

65. J. A. Venables. Atomic processes in crystal growth. *Surf. Sci.* **299**–**300**, 798–817 (1994).

66. T. E. James, S. L. Hemmingson, T. Ito, & C. T. Campbell. Energetics of Cu Adsorption and Adhesion onto Reduced CeO2(111) Surfaces by Calorimetry. *J. Phys. Chem. C* **119**, 17209–17217 (2015).

67. Z. Mao, J. R. Rumptz, & C. T. Campbell. Energetics of Ag Adsorption on and Adhesion to Rutile TiO2(100) Studied by Microcalorimetry. *J. Phys. Chem. C* **125**, 3036–3046 (2021).

68. W. Tian, H. P. Sun, X. Q. Pan, J. H. Yu, M. Yeadon, C. B. Boothroyd, Y. P. Feng, R. A. Lukaszew, & R. Clarke. Hexagonal close-packed Ni nanostructures grown on the (001) surface of MgO. *Appl. Phys. Lett.* **86**, 131915 (2005).

69. J. Higuchi, M. Ohtake, Y. Sato, T. Nishiyama, & M. Futamoto. Preparation and Structural Characterization of hcp and fcc Ni Epitaxial Thin Films on Ru Underlayers with Different Orientations. *Jpn. J. Appl. Phys.* **50**, 63001 (2011).

70. M. Ohtake, Y. Sato, J. Higuchi, & M. Futamoto. Microstructure of hcp-Ni(1100)/bcc-Cr(211) Bi-layer Film Grown on MgO(110) Substrate. in *Journal of Physics: Conference Series* **266**, 012122 (2011).

71. M. Ohtake, Y. Sato, J. Higuchi, T. Tanaka, F. Kirino, & M. Futamoto. Epitaxial growth of metastable hcp-Ni and hcp-NiFe thin films on Au (100) fcc single-crystal underlayers and their structure characterization. *Jpn. J. Appl. Phys.* **50**, 103001 (2011).

72. J. Y. Hwang, A. R. P. Singh, M. Chaudhari, J. Tiley, Y. Zhu, J. Du, & R. Banerjee. Templated growth of hexagonal nickel carbide nanocrystals on vertically aligned carbon nanotubes. *J. Phys. Chem. C* **114**, 10424–10429 (2010).

73. H. Cheng, N. Yang, Q. Lu, Z. Zhang, & H. Zhang. Syntheses and properties of metal nanomaterials with novel crystal phases. *Adv. Mater.* **30**, 1707189 (2018).

74. S. Illy, O. Tillement, F. Machizaud, J. M. Dubois, F. Massicot, Y. Fort, & J. Ghanbaja.

First direct evidence of size-dependent structural transition in nanosized nickel particles. *Philos. Mag. A* **79**, 1021–1031 (1999).

75. J. Singh, Tarachand, S. S. Samatham, D. Venkateshwarlu, N. Kaurav, V. Ganesan, & G. S. Okram. Quantum size effect on the heat capacity of nickel nanolattice. *Appl. Phys. Lett.* **111**, 201904 (2017).

76. H. Lin, H. Lin, J. X. Liu, H. Fan, & W. X. Li. Compensation between Surface Energy and hcp/fcc Phase Energy of Late Transition Metals from First-Principles Calculations. *J. Phys. Chem. C* **124**, 11005–11014 (2020).

77. R.-T. Chiang, R.-K. Chiang, & F.-S. Shieu. Emergence of interstitial-atom-free HCP nickel phase during the thermal decomposition of Ni 3 C nanoparticles. *RSC Adv.* **4**, 19488–19494 (2014).

78. P. N. Plessow & C. T. Campbell. Influence of Adhesion on the Chemical Potential of Supported Nanoparticles as Modeled with Spherical Caps. (2022). doi:10.1021/acscatal.1c04633

79. S. C. Parker & C. T. Campbell. Kinetic model for sintering of supported metal particles with improved size-dependent energetics and applications to Au on TiO2 (110). *Phys. Rev. B - Condens. Matter Mater. Phys.* **75**, (2007).

80. C. T. Campbell, S. C. Parker, & D. E. Starr. The effect of size-dependent nanoparticle energetics on catalyst sintering. *Science* **298**, 811–814 (2002).

Table of Contents Image